

# Quantum technologies with optically interfaced solid-state spins

David D. Awschalom<sup>1,2\*</sup>, Ronald Hanson<sup>3,4</sup>, Jörg Wrachtrup<sup>5,6</sup> and Brian B. Zhou<sup>1,7</sup>

**Spins of impurities in solids provide a unique architecture to realize quantum technologies. A quantum register of electron and nearby nuclear spins in the lattice encompasses high-fidelity state manipulation and readout, long-lived quantum memory, and long-distance transmission of quantum states by optical transitions that coherently connect spins and photons. These features, combined with solid-state device engineering, establish impurity spins as promising resources for quantum networks, information processing and sensing. Focusing on optical methods for the access and connectivity of single spins, we review recent progress in impurity systems such as colour centres in diamond and silicon carbide, rare-earth ions in solids and donors in silicon. We project a possible path to chip-scale quantum technologies through sustained advances in nanofabrication, quantum control and materials engineering.**

Driven by the quest for efficiency, modern technologies developed through persistent miniaturization. Devices such as transistors, magnetic memories and lasers advanced by reducing the number of electrons used per gate, bit, or output photon. This progression's arrival at the quantum limit now inspires a new class of information processing hardware that starts with the quantum coherence of single charges, spins, or photons and grows by harnessing the inseparable connections among them. This reversal from scaling down to building up lies at the heart of radical technologies that promise breakthroughs in computational power, communications security and sensor detection limit.

Solid-state spins are a promising platform for realizing these quantum advantages because of their robustness to decoherence and compatibility with scalable device engineering<sup>1</sup>. In particular, this Review focuses on optically addressed electron and nuclear spins at impurities in crystals. In recent years, pioneering experiments have isolated single spins at these atomic-scale impurities and demonstrated high-fidelity initialization, manipulation and readout of their quantum states<sup>2</sup>. These advances at the single-qubit level establish a critical foundation, but the connectivity among multiple qubits is required to unlock their full potential. We highlight the capacity of hybrid quantum registers formed by an electron spin coupled to multiple nuclear spins in its proximity. Electron spins readily sense and interface to the outside environment, while nuclear spins provide well-isolated quantum memories. These complementary functionalities, accessed through the generation of entangled states, enable an array of applications, including photonic memories<sup>3</sup>, quantum repeaters<sup>4</sup>, error correction<sup>5</sup> and enhanced quantum sensing<sup>6</sup>.

We concentrate on solid-state spins that utilize optical electronic transitions to fulfil several of the DiVincenzo criteria for quantum information processing<sup>7</sup>. Optical pumping can directly initialize the electron spin and its coupled nuclear spins, or, alternatively, coherent manipulations can transfer optically generated electron spin polarization to nuclear memories<sup>8,9</sup>. Additionally, spin-dependent optical

cycles correlate spin information to photon emission, enabling sensitive readout of spin states. Such remarkable optical properties of defect systems have been combined with techniques adapted from atomic physics and magnetic resonance to enable experiments on single electron and nuclear spins at ambient conditions, surpassing limitations in the original fields. Moreover, spin-selective optical transitions, accessed at cryogenic temperatures, coherently map between the quantum states of local spins and propagating photons<sup>10,11</sup>. This light/matter interface establishes each electron as a quantum gateway to distribute and process entanglement between distant registers in a quantum network.

We aim to provide an introduction and broad update on optically active impurity systems, emphasizing the partnership between electron and nuclear spins. We first describe the framework for manipulating hybrid quantum registers in the context of the prototype defect system, the nitrogen–vacancy (NV) centre in diamond<sup>8</sup>. We briefly review the optical and coherence properties of the NV electron spin, which provides access to the entire register. This discussion identifies the nuclear spin bath as the dominant source of decoherence, but leads to the opportunity to control selected nuclear memories via their distinct hyperfine interaction. We then overview emerging impurity systems, including alternative colour centres in diamond and silicon carbide, rare-earth ions in solids and optically active donors in silicon. These platforms offer unique advantages, such as in their optical properties or integrability with electronic or photonic devices, and stand to benefit from techniques developed for the NV centre. Then, we focus on technological applications of registers of quantum memories, ranging from quantum communication, computing and sensing. We conclude our Review by looking ahead to future challenges and progress with impurity spins in solids.

We remark that spins in self-assembled<sup>12,13</sup> and gate-defined quantum dots<sup>14</sup> share many parallel directions with impurity spins, including achievement of extended coherence times and enhanced light–matter coupling to enable multi-qubit interactions and

<sup>1</sup>Institute for Molecular Engineering, University of Chicago, Chicago, IL, USA. <sup>2</sup>Institute for Molecular Engineering and Materials Science Division, Argonne National Laboratory, Argonne, IL, USA. <sup>3</sup>QuTech, Delft University of Technology, Delft, The Netherlands. <sup>4</sup>Kavli Institute of Nanoscience, Delft University of Technology, Delft, The Netherlands. <sup>5</sup>Institute for Quantum Science and Technology IQST, and 3. Physikalisches Institut, University of Stuttgart, Stuttgart, Germany. <sup>6</sup>Max Planck Institute for Solid State Research, Stuttgart, Germany. <sup>7</sup>Present address: Department of Physics, Boston College, Chestnut Hill, MA, USA. \*e-mail: [awsch@uchicago.edu](mailto:awsch@uchicago.edu)

single-photon nonlinearities. The rapidly advancing state of the art in this field is, however, beyond the scope of our discussion. Likewise, we will overlook two-dimensional material systems, such as transition metal dichalcogenides and hexagonal boron nitride, that have recently emerged as hosts for single quantum emitters<sup>15–17</sup>. For these materials, explorations towards using the valley or spin degree of freedom of excitons or defect states as qubits are still in their infancy, but could open functionalities for quantum photonics, optoelectronics and sensing unattainable in bulk materials.

### The nitrogen-vacancy centre in diamond

Consisting of a substitutional nitrogen impurity adjacent to a missing carbon atom, the negatively charged NV centre in diamond traps six electrons at localized atomic-like states, protected from charge scattering by diamond's wide bandgap (Fig. 1a). NV centres display room-temperature quantum coherence, spin–photon entanglement and functionality inside engineered nanostructures, establishing their versatility for quantum information processing and nanoscale sensing.

**The electron spin and its optical interface.** The NV electron spin can be off-resonantly excited from its spin-triplet ground state (GS) to a spin-triplet, orbital-doublet excited state (ES) via phonon-assisted optical absorption<sup>8</sup>. Owing to a non-radiative, spin-flip decay channel that preferentially couples to the  $m_s = \pm 1$  sublevels of the excited state, repeated optical cycling initializes the electron spin into the  $m_s = 0$  level ( $\sim 90\%$  polarization)<sup>18</sup>. Concurrently, off-resonant excitation of  $|m_s = \pm 1\rangle$  results in  $\sim 30\%$  lower photoluminescence (PL) than  $|m_s = 0\rangle$ , allowing optical determination of the spin state at room temperature<sup>19</sup>. Higher-fidelity initialization and readout are obtained by cooling diamond below 10 K, where distinct spin-selective, zero-phonon optical transitions are resolved<sup>18</sup> (Fig. 1b). Resonant optical pumping of a spin-mixed transition (for example  $|m_s = \pm 1\rangle \rightarrow |A_1\rangle$ ) fully initializes the NV centre into  $|m_s = 0\rangle$  ( $>99.7\%$  polarization)<sup>18</sup>. Alternatively, by resonant excitation of a cycling transition ( $|m_s = 0\rangle \rightarrow |E_x\rangle$  or  $|E_y\rangle$ ) and optimizing photon-collection efficiency, the electron spin state can be determined without averaging multiple preparations ( $>97\%$  fidelity averaged for  $|m_s = 0\rangle$  and  $|m_s = \pm 1\rangle$ )<sup>20</sup>. Such single-shot measurements can be non-demolition to allow initialization of electron and nuclear spins by projective measurement<sup>18</sup>. Moreover, these spin-dependent optical transitions and their polarization selection rules form the basis for spin–photon entanglement<sup>10,11</sup>.

Aided by diamond's high Debye temperature and low spin–orbit coupling, NV centres possess long spin–lattice relaxation times  $T_1$  that reach  $\sim 5$  ms at room temperature and exceed hours at cryogenic temperatures ( $\sim 25$  mK)<sup>21,22</sup>. In high-quality samples grown by chemical vapour deposition, low concentrations of paramagnetic impurities leave the bath of  $^{13}\text{C}$  nuclear spins (1.1% natural abundance) as the dominant magnetic noise<sup>19</sup>. This dephasing can be mitigated in isotopically enriched materials ( $>99.99\%$   $^{12}\text{C}$ ). For single spins in isotopically purified samples, the inhomogeneous dephasing time  $T_2^*$ , reflecting temporal magnetic fluctuations, exceeds 100  $\mu\text{s}$  at room temperature<sup>23</sup>. Dynamical decoupling further filters the noise spectrum and extends spin coherence to the homogeneous dephasing time  $T_2$  of several milliseconds at room temperature<sup>24</sup> and nearly seconds at low temperature, limited by direct lattice contributions to spin dephasing ( $T_2 \approx 0.5T_1$ )<sup>25</sup> (Fig. 1c). These remarkable coherence times underpin the technological promise of NV centres, extending the range of this defect's access to nearby nuclear spins and enhancing its sensitivity to environmental influences.

**Strongly coupled nuclear spins.** While the nuclear bath represents the main contribution to electron spin decoherence, individual nuclear spins with isolated interactions offer a resource for quantum memories and multi-qubit entanglement<sup>9,26,27</sup>. Strongly

coupled nuclear spins, such as the intrinsic N forming the NV centre and proximal  $^{13}\text{C}$  atoms, possess hyperfine couplings larger than the electron spin resonance (ESR) linewidth, set by the dephasing rate  $1/T_2^*$  (Fig. 1a,d). For samples with natural isotope abundance, strongly coupled nuclei typically occur within 1 nm from the electron and have hyperfine couplings from 300 kHz to 130 MHz, where the latter value corresponds to a  $^{13}\text{C}$  on a nearest-neighbour lattice site<sup>28</sup>. For these nuclei, narrow-band microwave pulses at the distinct ESR transition frequencies (Fig. 1d) perform rotations of the electron spin conditional on the nuclear spin state (for example, controlled NOT gate,  $C_n\text{NOT}_e$ , where the subscripts n and e denote the nuclear and electron spin, respectively). Moreover, radio-frequency pulses can directly drive nuclear spin transitions ( $\Delta m_1 = \pm 1$ ) conditional on the electron spin manifold (for example,  $C_n\text{NOT}_n$ )<sup>29</sup>. Nuclear rotations can alternatively be implemented by nuclear Larmor precession for orthogonal nuclear quantization axes in different electron manifolds<sup>9</sup>. Using tailored pulse sequences of controlled two-qubit operations, the electron polarization can be transferred to the nuclear spin, after which the electron spin is reset by optical pumping<sup>9,30</sup>.

Readout of the nuclear spin is achieved by mapping its population and coherences onto the electron spin using a combination of selective radio-frequency and microwave pulses<sup>26</sup>. In ref. <sup>31</sup>, single-shot readout of the nuclear spin at room temperature was demonstrated by repeated application of electron–nuclear correlation ( $C_n\text{NOT}_e$ ) and optical readout of the electron (Fig. 1e). This repetition leverages the robustness of the nuclear spin to optical excitation to accumulate sufficient photon statistics. Projective readout can initialize multiple strongly coupled nuclei if the  $C_n\text{NOT}_e$  logic is conditional on each nuclear spin state of the multi-qubit register<sup>18</sup>.

The coherence times of nuclear spins and their sensitivity to optical illumination determine their usefulness as quantum memories. Nuclear coherence times  $T_{2n}$  exceed several milliseconds at room temperature and are limited by the electron spin relaxation time  $T_1$  and interactions with other nuclei<sup>9</sup>. Control over the NV charge state, either by strong optical illumination<sup>32</sup> or electrostatic gating<sup>33</sup>, can effectively decouple or eliminate the electron spin, extending nuclear  $T_{2n}$  beyond several seconds by the former technique. For nuclear depolarization ( $T_{1n}$ ), transverse components of the hyperfine interaction drive electron–nuclear flip-flops. Since hyperfine interactions may be stronger in the excited state, optical excitation can exacerbate depolarization, requiring high magnetic fields to minimize this process for strongly coupled nuclear spins<sup>31</sup>. In addition, these transverse terms become dominant near the excited-state anti-crossing ( $B \approx 500$  G), enabling optical excitation to drive dynamic nuclear polarization (DNP)<sup>34,35</sup>. The DNP efficiency can approach unity, depending on the strength and direction of the hyperfine interaction<sup>36</sup>. For quantum networks and error-corrected quantum computing, the coherences of nuclear spins must also be conserved under all operations performed with the electron spin<sup>37</sup>. Failed remote entanglement attempts due to photon loss or errors in the electron spin readout randomize the electron spin, introducing an uncertainty to the nuclear memory's precession frequency and accumulated phase that cannot be refocused. Hence, these considerations have motivated the exploration of more distant nuclear memories that are less sensitive to electronic interference.

**Weakly coupled nuclear spins.** Access to nuclear spins with hyperfine couplings weaker than  $1/T_2^*$  greatly increases the available number of register qubits and improves the longevity of each memory, at the expense of slower control speeds. This objective was achieved using dynamical decoupling (DD) sequences on the electron, thereby both extending its coherence and isolating its interaction with a particular nuclear spin<sup>23,38,39</sup>. The precession axis and frequency of a nuclear spin are conditional on the electron spin state and on its distinct hyperfine tensor (Fig. 1f). DD pulses that invert

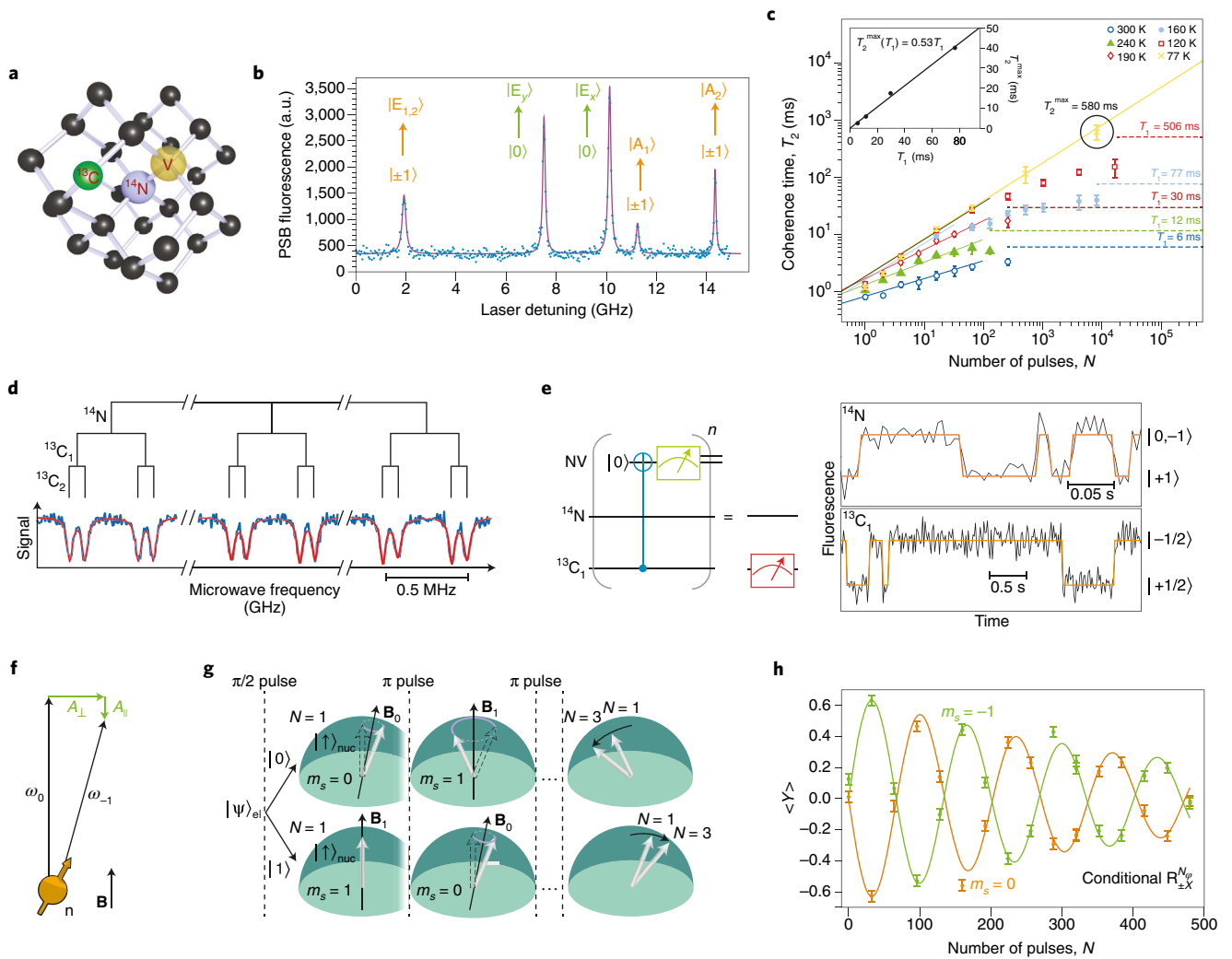


**Fig. 1 | The NV centre in diamond and nearby nuclear spins.** **a**, Schematic of an NV<sup>-</sup> centre in diamond. The NV electron spin is coupled to proximal nuclear spins, such as its intrinsic <sup>14</sup>N and lattice <sup>13</sup>C. **b**, PL into the phonon sideband (PSB) as the detuning of a laser is scanned across the NV centre ZPL (637.2 nm,  $T = 7$  K). Resonant transitions to six spin-orbit excited states follow spin-selection rules and enable optical spin initialization, readout and entanglement. Cycling transitions are labelled in green, whereas non-cycling transitions are labelled in orange. **c**, Coherence time  $T_2$  of an NV centre ensemble in isotopically purified diamond (0.01% <sup>13</sup>C) as a function of the number of pulses  $N$  in a dynamical decoupling sequence, for various temperatures. The inset depicts the relationship between the maximum coherence time  $T_2$  under dynamical decoupling and the spin relaxation time  $T_1$  at the same temperature. **d**, Optically detected magnetic resonance (ODMR) spectrum taken by sweeping the frequency of a microwave field and measuring the NV centre PL. The NV electronic transition  $|m_s = 0\rangle$  to  $|m_s = -1\rangle$  is split due to interaction with three strongly coupled nuclear spins (hyperfine couplings: <sup>14</sup>N, 2.16 MHz; <sup>13</sup>C<sub>1</sub>, 413 kHz; <sup>13</sup>C<sub>2</sub>, 89 kHz). **e**, Left: single-shot readout for strongly coupled nuclear spins (depicted by red box in ‘wire diagram’). The protocol consists of repetitions of the following block: the nuclear spin state (here for <sup>13</sup>C<sub>1</sub>) is correlated to the electron spin state by a controlled-not operation and then the electron state is read-out (green box). Right: fluorescence time traces showing quantum jumps between nuclear spin states. The orange curves are guides to the eye. **f**, Illustration of hyperfine coupling. If the electron spin is in  $|m_s = 0\rangle$ , the nuclear spin (labelled ‘n’) precesses with frequency  $\omega_0$  about the applied magnetic field **B**, while in  $|m_s = -1\rangle$ , the nuclear precession frequency  $\omega_{-1}$  and axis are modified by the hyperfine components  $A_{||}$  and  $A_{\perp}$ , which depend on the relative position between the nuclear and electron spin. **g**, Schematic for the evolution of a nuclear spin when the electron spin is repeatedly flipped by a dynamical decoupling sequence. **B**<sub>0</sub> and **B**<sub>1</sub> are the effective magnetic fields felt by the nuclear spin when the electron spin state  $|\psi\rangle_{el}$  is  $|m_s = 0\rangle$  and  $|m_s = 1\rangle$ , respectively. When the spacing between the electronic  $\pi$ -pulses is in resonance with a half-period of the nuclear Larmor precession, the nuclear spin effectively rotates in opposite directions depending on the initial electron spin state. **h**, Data showing oscillations in the  $\langle Y \rangle$  component of a weakly coupled nuclear spin after a dynamical decoupling sequence. This sequence implements a conditional nuclear rotation gate  $R_{\pm X}^{N\varphi}$ : the initial electron spin state determines the nuclear rotation axis ( $\pm X$ ), while the number of pulses  $N$  determines the total rotation angle  $N\varphi$ . Figure reproduced from: **a**, ref. <sup>23</sup>, Springer Nature Ltd; **b**, ref. <sup>10</sup>, Springer Nature Ltd; **c**, ref. <sup>25</sup>, Springer Nature Ltd; **d, e**, ref. <sup>30</sup>, Springer Nature Ltd; **f**, ref. <sup>37</sup>, under a Creative Commons licence (<https://creativecommons.org/licenses/by/3.0/>); **g**, ref. <sup>38</sup>, APS; **h**, ref. <sup>40</sup>, Springer Nature Ltd.

the electron spin thus modulate the nuclear precession, such that when the unique dynamics of a targeted nuclear spin is in resonance with the periodicity of the DD pulses, the precession due to its transverse hyperfine component accumulates<sup>38,40</sup> (Fig. 1g). Meanwhile, destructive interference occurs for nuclear spins with dynamics

out-of-sync with the DD sequence. Through this method, universal control<sup>40</sup> and single-shot readout<sup>41</sup> of weakly coupled nuclear spins were demonstrated (Fig. 1h). These capabilities, together with remote electron entanglement<sup>11,42</sup>, establish an architecture for distributed quantum communication and computing based on

error-corrected few-qubit nodes. Moreover, the direct applicability of DD methods to sensing nuclear species external to diamond has impacted progress in nanoscale magnetic resonance<sup>43,44</sup>.

### Emerging systems for spin/light interfaces

Although possessing long spin coherence, NV centres are hindered by their broad emission spectrum, where only ~4% of the total photons are coherently emitted into the zero-phonon line (ZPL) at 6 K (ref. 45). Since entanglement protocols require indistinguishable photons from remote NVs, this low percentage and the high scattering losses in optical fibre at the ZPL wavelength (637 nm) have limited entanglement rates to 40 Hz (ref. 20). Achieving higher bandwidth in NV-based quantum networks will thus require photonic cavities to boost ZPL emission<sup>45–48</sup> and, for long-distance networks, quantum frequency conversion into telecom wavelengths<sup>49</sup>, together with the advantages of a quantum repeater architecture. Promising for quantum network applications, recent experiments at cryogenic temperatures have shown emission into the ZPL with 46% probability using microcavities<sup>50</sup> and conversion of single NV photons into telecom wavelength with 17% efficiency using difference frequency generation<sup>51</sup>. A parallel approach that may relax these requirements for efficient long-distance entanglement is the advancement of alternative colour centres with more favourable intrinsic properties.

### Silicon–vacancy and germanium–vacancy centres in diamond.

The silicon–vacancy (SiV) centre in diamond, consisting of an interstitial silicon atom midway between two adjacent carbon vacancies, has garnered interest as a higher-efficiency source of indistinguishable photons. The negative charge state SiV<sup>-</sup> features an orbital doublet in both the ground and excited states, with degeneracies broken by the spin–orbit interaction<sup>52,53</sup> (Fig. 2a). Four zero-phonon optical transitions between these orbital levels comprise over 70% of the total fluorescence emission, with ~50% into the single line C at 4 K (Fig. 2b). Moreover, due to the defect's inversion symmetry, SiV<sup>-</sup> optical transitions are robust in linear order to electric-field and strain variations, resulting in highly stable and homogeneous emission frequencies with lifetime-limited linewidths<sup>53</sup>.

The  $S = 1/2$  electronic spin of SiV<sup>-</sup> can be coherently controlled by either microwave or optical driving, where the latter utilizes a GS–ES lambda ( $\Lambda$ ) system tuned by an off-axis magnetic field. However, coherent population trapping<sup>54,55</sup> and Ramsey<sup>56</sup> experiments indicate a short spin dephasing time  $T_2^* \sim 100$  ns at 4 K. Phonon-mediated transitions between the two ground-state orbital branches, separated by 50 GHz ( $\approx 2.5$  K), represent the dominant contribution to spin dephasing, arising from slightly different spin splitting in each orbital. Recently, by cooling SiV<sup>-</sup> to 100 mK (refs 57,58), spin coherence was extended to  $T_2^* \approx 10$   $\mu$ s and  $T_2 \approx 13$  ms for an isotopically purified sample<sup>58</sup>, clearing the way for coherent manipulation of coupled nuclear memories. Additionally, efficient ZPL emission from SiV<sup>-</sup>, predominantly polarized into a single transition dipole, makes this defect attractive for coupling to nanophotonic structures<sup>59</sup>. Through precision placement of Si<sup>+</sup> ions into a nanophotonic cavity, the entanglement signature between two emitters was observed<sup>60</sup> (Fig. 2c). Possessing similar spin and optical properties as SiV<sup>-</sup>, the germanium–vacancy (GeV<sup>-</sup>) centre in diamond may offer stronger atom–light coupling due to its higher quantum efficiency<sup>61,62</sup>. Furthermore, the neutral charge state of SiV<sup>0</sup><sup>63,64</sup> and the tin–vacancy centre<sup>65,66</sup> have recently been investigated to potentially combine a robust optical interface with long spin coherence at moderate cryogenic temperatures, although optical spin readout for these systems has yet to be demonstrated.

**Divacancy and silicon–vacancy in silicon carbide.** Silicon carbide (SiC) presents an opportunity to integrate colour centres into a technologically mature platform capable of wafer-scale growth,

fabrication and doping<sup>67</sup>. Unlike diamond, SiC exists in over 250 polytypes<sup>68</sup> (different stacking sequences of a silicon–carbon bilayer unit) to allow customizable material properties and heterojunction devices, boosting the potential for interacting its hosted colour centre spins with electrical or mechanical degrees of freedom<sup>69,70</sup>. Among colour centres investigated in SiC, the divacancy and silicon–vacancy defects have fulfilled key requirements for quantum applications, including optical electron and nuclear spin addressability<sup>35,71</sup>, long spin coherence<sup>72–74</sup> and single-defect isolation<sup>72,75</sup>.

The neutral divacancy ( $V_C-V_{Si}$ ; missing C atom next to missing Si atom) possesses the same  $C_{3v}$  symmetry and number of active electrons as the NV centre in diamond, leading to analogous spin and optical structures<sup>67</sup> (Fig. 2d). Its spin-triplet ground state exhibits its electron coherence times  $T_2$  that can exceed 1 ms in samples with natural isotope abundance<sup>72</sup>. This extended coherence despite higher fractions of nuclear spins than diamond stems from the larger lattice spacing in SiC and the suppression of heteronuclear flip-flops between <sup>29</sup>Si and <sup>13</sup>C at moderate magnetic fields ( $T_2 > 1$  ms for  $B > 15$  mT)<sup>76,77</sup>. Crucially, divacancies have ZPLs at near-infrared wavelengths ( $\sim 1,100$  nm), where significantly lower attenuation in optical fibre ( $\sim 1$  dB km<sup>-1</sup> versus  $\sim 8$  dB km<sup>-1</sup> at 637 nm for the NV centre in diamond) will facilitate entanglement generation over long distances. Recently, single divacancies, isolated in the 4H and 3C polytypes, were shown to display well-resolved spin-dependent optical transitions below 20 K, similar to the NV centre (Fig. 2e)<sup>78</sup>. Consequently, high-fidelity resonant readout<sup>78</sup> of the divacancy spin (Fig. 2f) and Stark tuning of its optical transition frequencies<sup>79</sup> were demonstrated at cryogenic temperatures, establishing critical elements for the implementation of entanglement protocols<sup>11</sup>. Harnessing the advantages of divacancies for long-range quantum networks will also require improving their photon-collection efficiency and natural ZPL emission fraction (5–7%)<sup>78</sup>. To this end, 3C-SiC, which can be epitaxially grown as thin films on silicon, presents an advanced platform for nanophotonic engineering<sup>80,81</sup>.

The negatively charged silicon vacancy ( $V_{Si}$ ; single missing Si atom) diverges from the well-studied NV-type level structure due to its odd number of active electrons that gives rise to a  $S = 3/2$  ground state and a complex set of optical transitions<sup>82</sup>. Notably, its spin properties and optical readout at room temperature provide unique capabilities for thermometry<sup>83</sup> and vector magnetometry<sup>84</sup>. Single  $V_{Si}$  at both inequivalent lattice sites (V1 and V2 centres) in 4H-SiC have been isolated, with both centres possessing coherence on the order of milliseconds under dynamical decoupling<sup>73,74</sup> and the V1 centre emitting 40% of its photons into the ZPL at 4 K (ref. 74) (Fig. 2d,g). A crucial step will be the demonstration of the predicted excited-state fine structure<sup>82</sup> that enables schemes for spin–photon entanglement.

**Rare-earth ions in solids.** Owing to shielding provided by their filled outer electronic shells, rare-earth ions in solid-state crystals possess  $4f$  electrons with optical and spin levels that display narrow intrinsic linewidths and high spectral stability, reminiscent of free atoms. This isolation from environmental noise has been exploited in rare-earth ensembles for photonic quantum memories, where the quantum state of single photons is stored and retrieved via the collective optical and spin-wave excitations of the ensemble<sup>3,85</sup>. Moreover, rare-earth impurities provide exceptionally long-lived nuclear spins with relaxation and coherence times measured in units of days<sup>86</sup> and hours<sup>87</sup>, respectively. While these properties motivate rare-earth ensemble systems as leading platforms for quantum repeaters and transducers<sup>88,89</sup>, extending control to single rare-earth ions would expand capabilities for programmable quantum circuits.

Recently, several groups have optically addressed single rare-earth ions, overcoming challenges in signal-to-noise ratios due to their weak optical emission and high background fluorescence in low-purity samples. These groups implemented techniques such

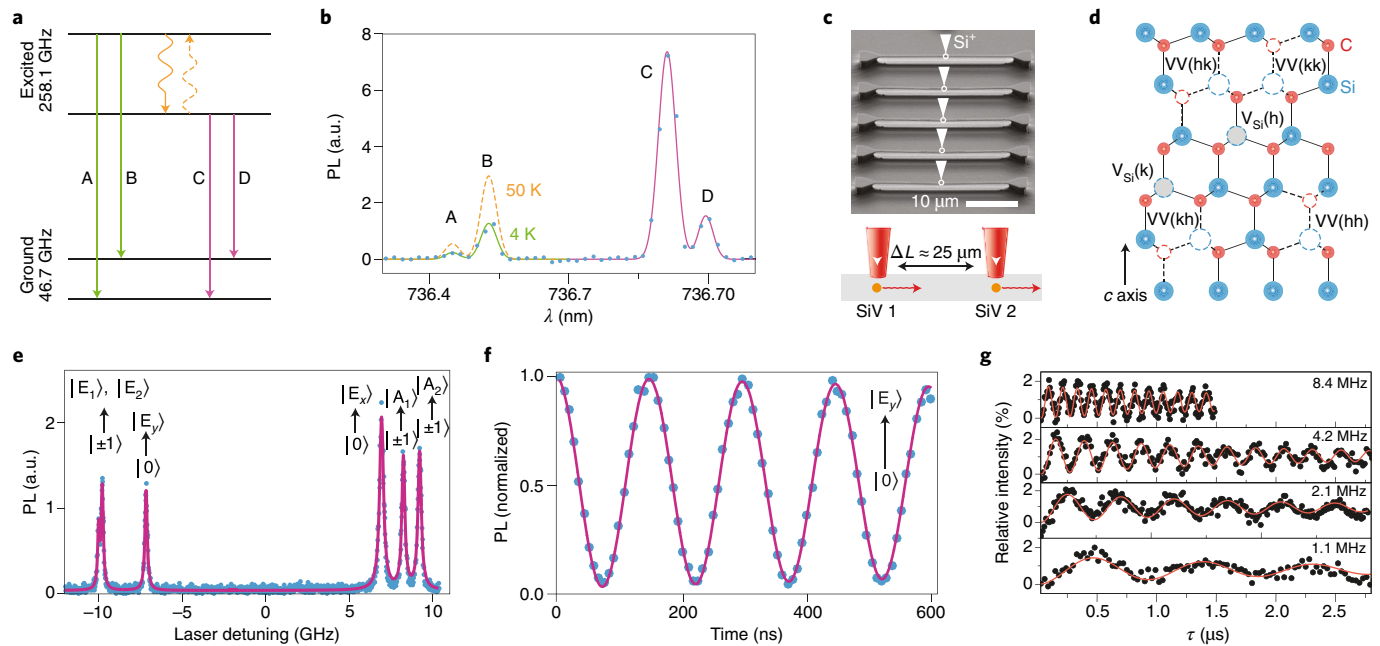


**Fig. 2 | The silicon-vacancy centre in diamond and colour centres in silicon carbide.** **a**, Orbital structure of the  $\text{SiV}^-$  centre, showing doublets in both the ground and excited states that are split by spin-orbit coupling. **b**, PL spectrum of the  $\text{SiV}^-$  centre in diamond, displaying four zero-phonon lines corresponding to transitions labelled in **a** (linewidths shown are limited by spectrometer resolution). The  $\text{SiV}^-$  centre's high Debye–Waller factor (~70% of total emission into ZPLs at 4 K), lifetime-limited optical linewidths and robustness to spectral diffusion make it an attractive source for indistinguishable photons. **c**, Scanning electron micrograph (SEM) of diamond nanophotonic cavities with  $\text{SiV}$  centres incorporated by precision ion implantation (top). The orbital states of two  $\text{SiV}$  centres (orange circles) separated by a distance  $\Delta L$  can be entangled by the emission of a single indistinguishable Raman photon into a nanophotonic waveguide (bottom). This entangled state is observed by its enhanced photon scattering statistics. **d**, Structure of 4H-SiC, showing two non-equivalent atomic sites for the Si and C atoms. h, quasihexagonal; k, quasicubic. There are two inequivalent forms of the silicon vacancy ( $V_{\text{Si}}$ ) and four inequivalent forms of the divacancy ( $V_{\text{C}}V_{\text{Si}}$ ) in 4H-SiC. **e**, PL excitation measurement (blue points) by scanning the detuning of a laser about the ZPL of a single divacancy (hh) in 4H-SiC (1,132 nm,  $T = 8$  K). The excited-state fine structure and optical spin-selection rules are analogous to the NV centre in diamond, but involve photons with near-telecom wavelengths. **f**, Rabi oscillation of a single divacancy spin (blue points). The high readout contrast of 94% is enabled by resonant excitation of the  $|0\rangle \rightarrow |E_y\rangle$  cycling transition. In **e,f**, the pink curves are fits to the data. **g**, Room-temperature Rabi oscillations (black points) of a single silicon vacancy spin ( $V_2$  centre) in 4H-SiC as a function of microwave power. Red curves are fits to the data. Figure reproduced from: **a,b**, ref. <sup>53</sup>, Springer Nature Ltd; **c**, ref. <sup>60</sup>, AAAS; **d**, ref. <sup>72</sup>, Springer Nature Ltd; **e,f**, ref. <sup>78</sup>, under a Creative Commons licence (<https://creativecommons.org/licenses/by/4.0/>); **g**, ref. <sup>75</sup>, Springer Nature Ltd.

as spectral isolation in microcrystallites<sup>90,91</sup>, customized optics to minimize the confocal volume<sup>92</sup> and fluorescence upconversion to levels with shorter optical lifetimes<sup>93</sup>. Coherent control over single  $\text{Ce}^{3+}$  electron spins in yttrium aluminium garnet (YAG) was demonstrated<sup>94</sup>. Additionally, the hyperfine levels of single  $\text{Pr}^{3+}$  ions in yttrium orthosilicate (YSO)<sup>90,91</sup>,  $\text{LaF}_3$  (ref. <sup>92</sup>) and YAG<sup>95</sup> were spectroscopically resolved, allowing nuclear spins to be initialized and read-out by resonant optical excitation and manipulated by radio-frequency fields (Fig. 3a,b). Coherence of single nuclear spins in Pr:YAG was limited at 4 K by electron–phonon coupling<sup>95</sup> ( $T_{1n} \sim 4$   $\mu\text{s}$ ), but can exceed seconds for Pr:YSO based on ensemble measurements<sup>96</sup>. Notably, an alternative detection route for single rare-earth ions relies on charge sensing of resonant photoionization, demonstrated for single  $\text{Er}^{3+}$  ions in a silicon single-electron transistor<sup>97</sup>.

The robustness of rare-earth systems to surface perturbations motivates nanophotonic engineering as a promising route to ameliorate their low photon count rate. Recently, an atomic frequency comb quantum memory with optical control over the storage time was demonstrated for a small ensemble of  $\text{Nd}^{3+}$  ions in a nanophotonic cavity<sup>98</sup>. Moreover, several groups reported addressing single rare-earth ions, exploiting cavity enhancement of their spontaneous emission rate (Purcell factors  $>100$ )<sup>99,100</sup>. Cavities can be fabricated directly into glassy rare-earth host materials by focused ion beam milling<sup>98,99</sup>. Additionally, they can be fabricated externally into a material, such as silicon, and then transferred onto the rare-earth

host for evanescent coupling<sup>100</sup>. These platforms set the stage for advances in optical control and remote entanglement of rare-earth electrons and nuclei, as well as quantum routing of single photons, in integrated photonic devices.

**Optically active donors in silicon.** The miniaturization of silicon electronics to the nanoscale has naturally broached the prospect for quantum systems in this technologically ubiquitous platform. In recent years, the electron and nuclear spins of single  $^{31}\text{P}$  donors in silicon have been read-out by spin-dependent tunnelling in a single-electron transistor, demonstrating state-of-the-art coherence times ( $T_{2e} > 0.5$  s at 100 mK) and control fidelities ( $>99.99\%$  for a single  $^{31}\text{P}$  nuclear spin)<sup>101</sup>. However, coupling between multiple donor qubits in silicon remains an unsolved challenge, motivating various proposals that span nanometre<sup>1</sup> to macroscopic length scales<sup>102,103</sup>. Schemes requiring strong coupling of individual donor spins to a common microwave resonator<sup>102</sup> are difficult to realize due to their small magnetic dipole moment. Recently, strong coupling between microwave cavity photons and a single electron spin in a silicon double quantum dot was achieved only after hybridizing the spin with its electronic wavefunction in the presence of an inhomogeneous magnetic field<sup>104,105</sup>. Alternatively, optical photon interconnects<sup>103</sup> could realize longer-distance couplings.

For group V shallow donors, optical transitions to excited orbital states occur in the far-infrared, a technologically difficult regime.

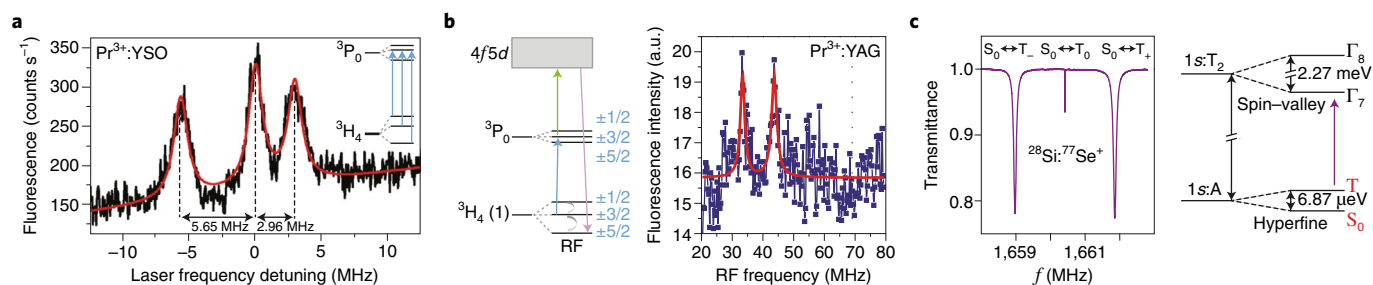


**Fig. 3 | Rare-earth ions in crystals and optically active donors in silicon.** **a**, Fluorescence excitation spectrum of a single  $\text{Pr}^{3+}$  ion in a YSO microparticle, resolving the hyperfine structure of the  $^3\text{P}_0$  excited state ( $T = 4$  K). **b**, ODMR for the ground-state hyperfine sublevels of a single  $\text{Pr}^{3+}$  ion in bulk YAG. Readout is achieved by a two-photon upconversion process (left). The relatively broad linewidths ( $\sim 2\pi \times 1.5$  MHz) of the ODMR peaks (blue points) indicate that the coherence of the  $\text{Pr}^{3+}$  nuclear spin in YAG is limited by spin-lattice relaxation at 4 K (right). RF, radio frequency. **c**, ODMR between the electron-nuclear spin singlet ( $S_0$ ) and triplet ( $T_-, T_0, T_+$ ) states of an ensemble of singly ionized  $^{77}\text{Se}$  double donors in silicon (left). Data are taken by first optically pumping the ensemble into the  $S_0$  state and then measuring the relative absorption of the  $T \leftrightarrow \Gamma_7$  transition (2,902 nm) at 2 K and in Earth's magnetic field (70  $\mu\text{T}$ ). The relevant ground ( $1s:A$ ) and excited-state ( $1s:T_2$ ) levels are shown in the right panel. Figure reproduced from: **a**, ref. <sup>91</sup>, under a Creative Commons licence (<https://creativecommons.org/licenses/by/3.0/>); **b**, ref. <sup>95</sup>, courtesy of Kangwei Xia; **c**, ref. <sup>103</sup>, AAAS, under a Creative Commons licence (<https://creativecommons.org/licenses/by-nc/4.0/>).

Instead, efforts have focused on transitions between the neutral donor ( $D^0$ ) and its donor-bound exciton ( $D^0X$ ) with energies at 1.15 eV, near bandgap. In isotopically enriched  $^{28}\text{Si}$  samples, these transitions are sufficiently narrow to resolve the hyperfine structure of  $^{31}\text{P}$  donors, allowing optical pumping through an Auger de-excitation to hyperpolarize the electron and nuclear spin<sup>106,107</sup>. This Auger decay occurs with near-unit probability in indirect-bandgap Si and enables electrical readout of long-lasting nuclear spin coherence that exceeds 39 min at room temperature for ensembles of ionized donors<sup>106,107</sup>. However, the non-radiative nature of this process precludes optical detection or coupling of single donors.

Recently, singly ionized, chalcogen double donors (for example,  $\text{S}^+$ ,  $\text{Se}^+$ ) have begun to be investigated for their stronger binding energies ( $\sim 600$  mV/2.9  $\mu\text{m}$ ) that permit donor optical transitions in the mid-infrared<sup>103</sup> (Fig. 3c). Optical measurements on  $^{77}\text{Se}^+$  ensembles at 1.2 K demonstrate competitive electron spin coherence times ( $T_{2,\text{Hahn}} = 2$  s for a qubit based on a clock transition) and hyperfine-resolved optical transitions with narrow homogeneous linewidths ( $< 29$  MHz). Isolation of single chalcogen donors in the future could enable the use of silicon-on-insulator photonics for cavity-enhanced readout and coupling<sup>103</sup>.

### Applications of quantum registers and memories

In this section, we highlight recent advances that leverage the collective functionality of electron and nuclear spins in solid-state defect systems for quantum applications.

**Quantum networks.** Shared entanglement between spatially separated nodes in a quantum network represents the essential resource for quantum key distribution and quantum cloud computing, possessing security independent of the trustworthiness of the communicating devices<sup>108</sup> or computing server<sup>109</sup>. Although photons are ideal long-distance carriers of quantum states, their conversion to long-lived stationary qubits is necessary for flexible timing of network tasks and efficient propagation of entanglement over long distances<sup>4</sup>. These requirements are fulfilled by the NV centre in diamond, which combines a spin/light interface with control over local nuclear memories. In 2013, a breakthrough experiment established entanglement between two NV spins separated by 3 m (ref. <sup>11</sup>). Using the Barrett-Kok protocol, each NV centre was prepared to allow probabilistic emission of a photon correlated with its spin state. If the NV centres emit indistinguishable photons (requiring the ZPL), overlapping their emitted modes on a beam-splitter erases which-path information and causes detection of a single photon to project

the NV centres into an entangled state. Owing to possible photon loss, detection of a second single photon in an ensuing trial where both NV spins are flipped is required to confirm the entangled state, leading to a low success probability  $P_E \approx 10^{-7}$ , proportional to the square of the photon-collection efficiency. Nevertheless, the high fidelity of the heralded entangled state ( $\sim 0.92$ ), as well as its fast tomography by single-shot readout, enabled the first loophole-free Bell test, using two NV centres separated by 1.3 km (ref. <sup>110</sup>) (Fig. 4a,b).

Incorporating nuclear memories with remote electron entanglement enables key network primitives, such as teleportation, entanglement purification and photonic quantum memory. The state of the nitrogen nuclear spin associated with one NV centre of an entangled pair was unconditionally teleported (that is, each attempt is successful) onto the electron spin of the other NV centre<sup>111</sup>. Recently, entanglement purification, an essential capability of quantum repeaters that 'distills' a single high-fidelity entangled state from multiple lower-fidelity copies, was achieved<sup>112</sup> (Fig. 4c,d). Here, a low-quality entangled state is first generated between two NV spins by detecting only a single output photon at the beam-splitter, forging the second trial of the Barrett-Kok protocol<sup>11,110</sup>. The entangled electron states are then swapped onto  $^{13}\text{C}$  nuclear spins at both nodes, freeing the communication qubits for additional entanglement generation. Critically, the weakly coupled nuclear memories used are robust to several hundred optical cycles of the electron<sup>27</sup>, allowing the second entanglement generation to be attempted until success. The memory qubits are finally projected onto a pure entangled state depending on the outcome of local operations on the two entangled pairs<sup>112</sup>. Since the purification protocol does not require simultaneous detection of single photons in two consecutive entanglement attempts, it achieves faster entanglement rates that scale linearly in photon detection probability.

While the above applications leverage the emission of spin-entangled photons, the optical interface of the NV centre additionally permits quantum storage of incident photons and absorption-based remote entanglement<sup>113</sup>. Raman quantum memories for photons similar to those for rare-earth and atomic systems were proposed for ensembles of NV centres<sup>114,115</sup>, but have been difficult to realize due to the crowded NV excited-state structure and larger optical inhomogeneous broadening. Alternatively, using a single NV centre, photon polarization states were coherently transferred onto the intrinsic nitrogen nuclear spin<sup>113</sup> (Fig. 4e,f). This recent demonstration prepares the electron and nitrogen nuclear spins in an entangled Bell state, and then utilizes the entangled absorption of

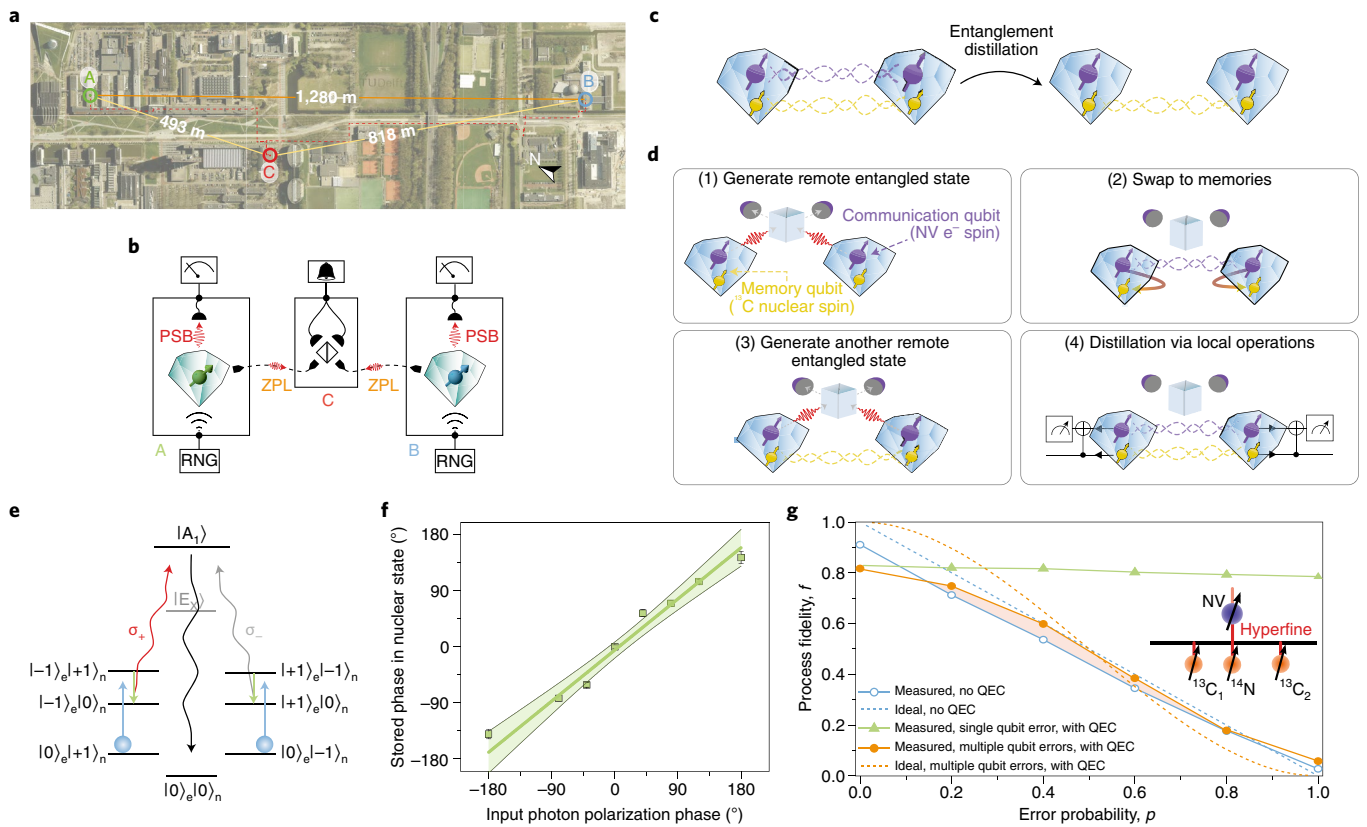


**Fig. 4 | Quantum registers for quantum networks and computing.** **a**, Photograph showing three lab stations A, B and C at the Delft University of Technology. An entangled state between two NV centres separated by 1.3 km (stations A and B) is generated by sending spin-entangled photons to station C. **b**, Experimental schematic for remote entanglement. Indistinguishable ZPL photons from NV centres at stations A and B are overlapped onto a beam-splitter at station C, where a particular sequence of single-photon detections heralds the generation of an entangled state. High-fidelity and fast single-shot spin readout enables a loophole-free test of the Bell inequality. RNG, random number generator. **c**, Principle of entanglement distillation. Two lower-quality remote entangled states can produce a single higher-fidelity entangled state through local operations and classical communication. **d**, Experimental implementation of entanglement distillation using an NV centre electron spin (communication qubit) and a weakly coupled  $^{13}\text{C}$  nuclear spin (memory qubit) at each node. The success of the distillation protocol, resulting in a higher-fidelity entangled state between the memory qubits, is probabilistic, but is heralded by a particular measurement outcome on the communication qubits. **e**, Scheme for storage of a photon polarization state by the  $^{14}\text{N}$  nuclear spin of the NV centre. The NV centre is first prepared in an electron–nuclear Bell state. At zero magnetic field, the electronic levels  $|\pm 1\rangle_e$  couple to  $|A_1\rangle$  by opposite circularly polarized light ( $\sigma_+$  and  $\sigma_-$ ) to form a degenerate  $\Lambda$  system. In this case, the entangled absorption of a resonant photon transfers the photon polarization onto the phase of the nuclear superposition state. Successful absorption is heralded by single-shot spin readout. **f**, Data showing the faithful mapping of the photon polarization onto the nuclear superposition state. Green shaded area is the 95% confidence interval. **g**, Quantum error correction using a register of three strongly coupled nuclear spins (schematically depicted in the inset). This code can surpass the fidelity of no error correction (blue circles) when a single error occurs of one of the qubits (green triangles) or when errors occur with equal probability on all three qubits (orange circles). Figure reproduced from: **a**, ref. <sup>110</sup>, Springer Nature Ltd/Slagboom en Peeters Luchtfotografie BV; **b**, ref. <sup>110</sup>, Springer Nature Ltd; **c,d**, ref. <sup>112</sup>, AAAS; **e,f**, ref. <sup>113</sup>, Springer Nature Ltd; **g**, ref. <sup>30</sup>, Springer Nature Ltd.

a photon in a degenerate optical  $\Lambda$  system<sup>116</sup> to teleport the photon polarization onto the nuclear spin. This approach paves the way for entanglement distribution between network nodes through the absorption of entangled photon pairs at the NV resonant energy.

**Quantum computing.** Overcoming the challenge of scaling a quantum computer to the large number of qubits required to outperform classical algorithms hinges on correcting the inevitable errors that arise due to the delicate, analogue nature of quantum states. While a potential resolution lies in a monolithic architecture employing a large qubit array stabilized by topological codes, a distributed or modular architecture that utilizes photonically linked nodes, each with only a small number of qubits, could provide efficiencies due to its reconfigurable connections and non-local quantum gates<sup>117</sup>. This distributed architecture is particularly applicable to defect-based quantum registers of electron and nuclear spins, which satisfy the requirements for inter-node photonic entanglement, as

well as intra-node universal control and non-demolition readout. Encouragingly, a distributed error-correction approach using only four qubits per node was shown to possess modest threshold error rates for the entangling links ( $\sim 10\%$ ) and local operations ( $\sim 1\%$ ) that would allow a large-scale implementation to be fault-tolerant<sup>118</sup>.

Experimental efforts have so far focused on error correction within individual nodes. In 2014, two groups<sup>30,40</sup> demonstrated a majority-vote error-correction protocol, encoding a quantum bit in a logical qubit of three spins (Fig. 4g). These experiments leveraged advanced electron–nuclear initialization sequences and quantum gates to correct a single bit-flip error automatically during the decoding of the three-qubit register, avoiding direct measurement of error syndromes. More recently, by utilizing non-demolition, single-shot readout at cryogenic temperatures, a stabilizer-based approach<sup>119</sup> involving active error detection and real-time feedback was implemented for a logical qubit of three weakly coupled  $^{13}\text{C}$  nuclei. This latter experiment demonstrated a continuously

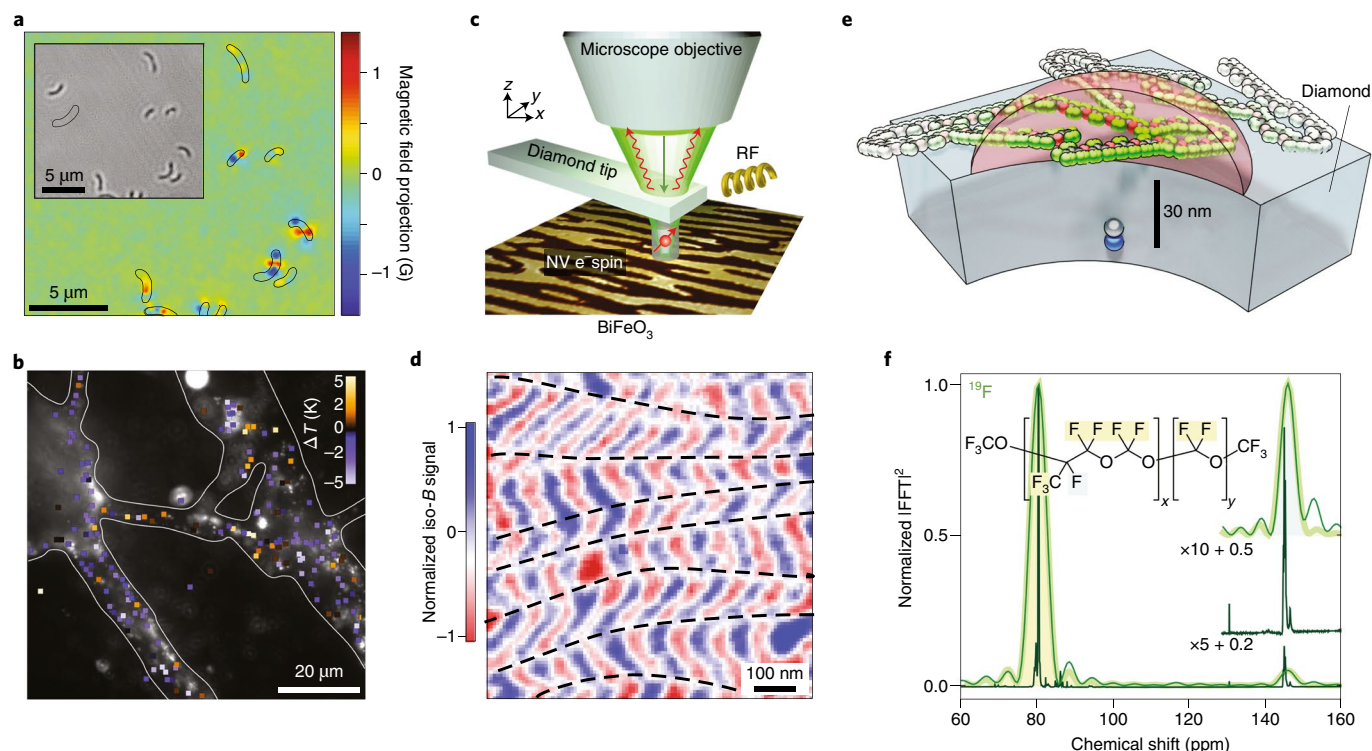


**Fig. 5 | Diverse modalities and applications of quantum sensing with impurity spins. a**, Wide-field magnetic imaging of magnetotactic bacteria on top of a dense array of shallow NV centres. The colour bar depicts the magnetic field projection along the [111] NV axis. The inset shows the bright-field image for the same region. **b**, Intracellular temperature map of primary cortical neurons using nanodiamonds (ND) incorporated by cellular uptake. The colour code denotes the change in measured temperature for each ND in response to a reduction in environmental temperature. **c**, An atomic force microscope using a diamond scanning tip with a single NV centre at its apex enables magnetic field imaging with a spatial resolution of tens of nanometres, determined by the NV-to-sample distance. RF, radio frequency. **d**, Magnetic stray field image capturing the non-collinear magnetic order of a multiferroic  $\text{BeFeO}_3$  thin film. The colour bar is related to the change in local magnetic field from a reference value. **e**, Geometry for NMR on nanoscale sample volumes with a near-surface NV magnetic sensor. **f**, NMR chemical shift for  $^{19}\text{F}$  nuclei in perfluoropolyether oil (chemical structure depicted in inset) detected by an NV spin (light green trace). The high spectral resolution of this experiment is achieved by using a long-lived nuclear memory to extend the phase acquisition time. For comparison, the dark green trace shows a spectrum taken by a conventional 400 MHz NMR spectrometer. Figure reproduced from: **a**, ref. <sup>123</sup>, Springer Nature Ltd; **b**, ref. <sup>124</sup>, American Chemical Society; **c,d**, ref. <sup>127</sup>, Springer Nature Ltd; **e,f**, ref. <sup>139</sup>, AAAS.

phase-corrected logical qubit with coherence exceeding its best component qubit. Future prospects include extending error correction to larger qubit registers and applying more sophisticated codes to repair arbitrary single-qubit errors, or combining it with remote electron entanglement for networked information processing. In addition, the potential to coherently interface shallow NV centres with chemically assembled nuclear spin arrays on the surface of diamond could enable large-scale quantum simulations<sup>120</sup>. Towards simulations of quantum chemistry and condensed-matter phases, proof-of-principle demonstrations with NV quantum registers internal to diamond have deduced the energy structure of a  $\text{HeH}^+$  cation<sup>121</sup> and a topological wire coupled to a superconductor<sup>122</sup>.

**Quantum sensing.** The atomic-scale dimensions, fast dynamics and acute sensitivity of quantum systems make them exceptional probes of their environment, combining high spatial resolution, bandwidth and precision. The challenge of quantum sensing is to isolate maximum information about a target variable from its effect on the dynamics of the quantum sensor, which simultaneously experiences decoherence and a multitude of competing influences<sup>6</sup>. The room-temperature coherence of NV centres and their diverse deployment inside wide-field arrays<sup>123</sup>, nanoparticles<sup>124</sup> and scanning probes<sup>125–127</sup> have precipitated their development as a transformative technology for sensing magnetic fields and other external perturbations (Fig. 5a–d). Wide-ranging efforts have leveraged the NV sensor for detection and characterization of intracellular and

biological processes<sup>123,124,128</sup>, nanoscale nuclear magnetic resonance (NMR)<sup>43,44,129,130</sup>, magnetism in condensed-matter systems<sup>125–127,131</sup> and device performance of nanotechnologies<sup>132,133</sup>.

In particular, NV detection of NMR spectroscopy significantly enhances the sensitivity and spatial resolution of this powerful technique, promising chemical structure identification with single-molecule sensitivity and subcellular resolution (Fig. 5e,f). However, improving the frequency resolution of NV detection to distinguish the few-hertz changes in NMR frequencies due to chemical shifts and spin–spin couplings represents an ongoing pursuit. Pioneering works applied DD sequences to single shallow NV centres to sense the magnetic field fluctuations from a statistical polarization of  $\sim 10^2$  external protons<sup>43,44</sup>. These experiments demonstrated  $\sim 10$  kHz NMR linewidths, limited by  $T_2$  of the NV sensor and diffusion of the target nuclei through the nanoscale sensing volume. Correlation spectroscopy extends the phase acquisition time to the electron  $T_1$  ( $\sim$ ms), improving spectral resolution to several hundred hertz<sup>134,135</sup>. Here, the phase accumulated during an initial DD segment is stored in the polarization of the electron spin and then correlated to the phase from a second DD segment after free evolution of the target nuclei.

Recently, the intrinsic nitrogen nuclear spin was leveraged as a longer-term memory for the initial phase measured in correlation spectroscopy, extending the interrogation time to  $T_{1n}$  ( $>$ minutes for tesla-scale magnetic fields)<sup>136–138</sup>. This approach naturally integrates repetitive, non-demolition nuclear state readout<sup>31,130</sup> and

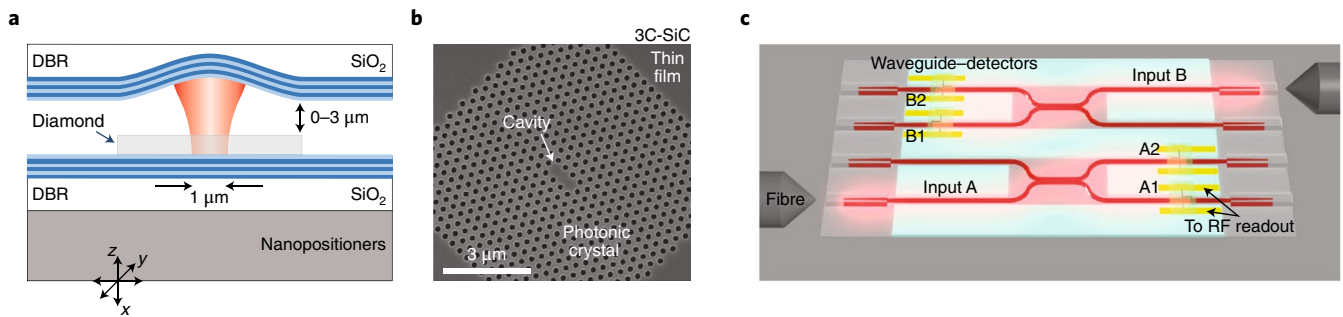


**Fig. 6 | Photonic engineering for solid-state spins. a**, Miniaturized Fabry-Pérot microcavity containing a thin diamond membrane. Nanopositioning a movable distributed Bragg reflector (DBR) mirror allows in situ tuning of the cavity resonance frequency and antinode location. Emission of the NV centre into the ZPL is boosted to 46% at 4 K. **b**, SEM image of a photonic crystal cavity in 3C-SiC. The starting material is grown as a heteroepitaxial thin film on silicon, allowing for effective substrate removal. Collected PL from a divacancy ensemble in the cavity is enhanced by a factor of 30. **c**, Implementation of a photonic integrated circuit featuring on-chip waveguides and superconducting nanowire single-photon detectors (A1, A2, B1, B2). This architecture could provide a route towards scalable on-chip entanglement of impurity spins. Figure reproduced from: **a**, ref. <sup>50</sup>, under a Creative Commons licence (<https://creativecommons.org/licenses/by/4.0/>); **b**, ref. <sup>81</sup>, APS; **c**, ref. <sup>148</sup>, under a Creative Commons licence (<https://creativecommons.org/licenses/by/4.0/>).

also frees the sensor electron spin so that its back-action on the target nuclei, which shortens their correlation time, can be decoupled<sup>137</sup>. Although sample diffusion still limited the sensing duration (~5 ms), the nuclear memory approach resolved part-per-million-level chemical shifts in liquid-state samples<sup>139</sup> (Fig. 5f). Alternatively, a recent NMR scheme<sup>140</sup> utilized an NV ensemble and a synchronous readout technique<sup>141,142</sup> that enabled frequency resolution independent of the sensor coherence time. Here, the larger sensing volume mitigated the effects of diffusion and enabled access to the thermal, rather than statistical, nuclear polarization, culminating in ~3 Hz spectral resolution to resolve chemical shifts and nuclear spin-spin couplings<sup>140</sup>.

### Challenges and outlook

Even with the enormous progress in impurity systems, the potential for improvement across the spectrum of applications is limitless. Realizing kilohertz entanglement rates across metropolitan distances, distributed logical qubits in a fault-tolerant network, or real-time intracellular NMR spectroscopy, among other far-reaching goals, will require concerted advances in photonic and device engineering, quantum control and materials science. Moreover, while it may be enticing to regard solid-state spins as a self-sufficient platform, exploration of their connection to diverse quantum systems may lead to hybrid devices with optimized components. Recent advances in interacting NV spins with microwave<sup>143</sup>, acoustic<sup>144,145</sup>, or magnonic excitations<sup>146,147</sup> open new routes towards on-chip state transfer and entanglement between impurity spins or hybrid systems.

While the solid-state environment poses challenges to impurity spins via phonon broadening and total internal reflection of their emission, it also provides them their greatest asset, amenability to fabrication and device integration. Coupling of optical emitters to photonic cavities with high quality factors and small mode volumes concentrates their emission into the ZPL and into a single cavity mode for efficient collection. A recent Fabry-Pérot microcavity design<sup>50</sup> directs 46% of the NV centre's emission into the ZPL, offering in situ resonance tuning and reduced processing-induced broadening of NV linewidths as advantages over previous monolithic diamond approaches<sup>46</sup> (Fig. 6a). In parallel, novel defect platforms with robust ZPLs<sup>60</sup> or advanced heteroepitaxy and selective etching techniques<sup>78</sup> will accelerate photonic cavity development (Fig. 6b). These advances will enable significantly higher rates of indistinguishable photons for long-distance entanglement, as well as ultimately near-deterministic light-matter interactions in the strong-coupling regime of cavity quantum electrodynamics.

Towards continental-scale fibre-based quantum networks, defect systems with near-telecom wavelength emission, such as divacancies in SiC or various rare-earth ions, may offer additional avenues to create efficient entanglement between solid-state nodes.

At a more local level, a promising direction lies in integrating impurity spins with on-chip photonics, thereby creating field-deployable quantum sensors and compact information processing devices. An integrated package using microfabricated photonic elements, including waveguides, couplers, metalenses and superconducting nanowire detectors, could crucially reduce optical losses and eliminate bulky free-space optics<sup>48,148,149</sup> (Fig. 6c). In these integrated photonic circuits, impurity spins would provide powerful functionalities as single-photon sources, photonic memories and nonlinear single-photon switches, establishing a scalable architecture for quantum processors based on either photonic or modular matter-based qubits. Moreover, engineering of lab-on-a-chip devices<sup>150</sup> and deployable probes, such as nanodiamonds attached directly to optical fibres<sup>51</sup>, will proliferate the reach of quantum sensing. For example, diamond devices with surface-structured microfluidic grooves realize both enhanced sensor-analyte contact for NMR applications and increased photon-collection efficiency by optical waveguiding<sup>152</sup>.

Advances in quantum control and materials science will naturally be fundamental to continued progress. Encoding quantum memories in decoherence-free subspaces of two nuclear spins would allow the use of more strongly coupled nuclear spins while maintaining robustness to optical excitation<sup>37</sup>. This would increase speeds for interfacing quantum memories and enable high-throughput multiplexed versions of entanglement protocols, where entanglement is continuously attempted using multiple memories before successes are heralded<sup>153</sup>. Time-dependent Hamiltonian engineering, such as optimal control<sup>154</sup> and shortcuts to adiabaticity<sup>155</sup>, could be extended for fast and robust gates despite densely spaced electron-nuclear energy levels. Furthermore, the convergence of quantum error correction and quantum sensing could improve sensitivity by extending qubit coherence regardless of the noise spectrum, in contrast to dynamical decoupling. Pioneering demonstrations<sup>156,157</sup> leveraged a single ancilla nuclear spin that is robust against noise to correct the NV electron sensor. Finally, improvements in materials engineering could overcome current limits to many applications, as well as open new opportunities. Important challenges include the creation of high-density near-surface defect centres with long coherence times and a single orientation<sup>158–160</sup>, control over defect charge states by Fermi level tuning, and customized surface functionalization for targeted sensing tasks. In addition, the discovery of novel impurity

systems with superlative optical, spin and host material properties may aid in bringing solid-state spins closer to widely impactful quantum technologies.

Received: 6 February 2018; Accepted: 12 July 2018;

Published online: 29 August 2018

## References

- Kane, B. E. A silicon-based nuclear spin quantum computer. *Nature* **393**, 133–137 (1998).
- Hanson, R. & Awschalom, D. D. Coherent manipulation of single spins in semiconductors. *Nature* **453**, 1043–1049 (2008).
- de Riedmatten, H. & Afzelius, M. in *Engineering the Atom-Photon Interaction* (eds Predojević, A. & Mitchell, M. W.) 241–273 (Springer, Cham, Switzerland, 2015).
- Munro, W. J., Azuma, K., Tamaki, K. & Nemoto, K. Inside quantum repeaters. *IEEE J. Sel. Top. Quantum Electron.* **21**, 78–90 (2015).
- Terhal, B. M. Quantum error correction for quantum memories. *Rev. Mod. Phys.* **87**, 307–346 (2015).
- Degen, C. L., Reinhard, F. & Cappellaro, P. Quantum sensing. *Rev. Mod. Phys.* **89**, 035002 (2017).
- DiVincenzo, D. P. The physical implementation of quantum computation. *Fortschritte Phys.* **48**, 771–783 (2000).
- Doherty, M. W. et al. The nitrogen-vacancy colour centre in diamond. *Phys. Rep.* **528**, 1–45 (2013).
- Dutt, M. V. G. et al. Quantum register based on individual electronic and nuclear spin qubits in diamond. *Science* **316**, 1312–1316 (2007).
- Togan, E. et al. Quantum entanglement between an optical photon and a solid-state spin qubit. *Nature* **466**, 730–736 (2010).
- Bernien, H. et al. Heralded entanglement between solid-state qubits separated by three metres. *Nature* **497**, 86–90 (2013).
- Warburton, R. J. Single spins in self-assembled quantum dots. *Nat. Mater.* **12**, 483–493 (2013).
- Lodahl, P. Quantum-dot based photonic quantum networks. *Quantum Sci. Technol.* **3**, 013001 (2018).
- Vandersypen, L. M. K. et al. Interfacing spin qubits in quantum dots and donors—hot, dense, and coherent. *npj Quantum Inf.* **3**, 34 (2017).
- Aharonovich, I., Englund, D. & Toth, M. Solid-state single-photon emitters. *Nat. Photon.* **10**, 631–641 (2016).
- Shiue, R. J. et al. Active 2D materials for on-chip nanophotonics and quantum optics. *Nanophotonics* **6**, 1329–1342 (2017).
- Atature, M., Englund, D., Vamivakas, N., Lee, S.-Y. & Wrachtrup, J. Material platforms for spin-based photonic quantum technologies. *Nat. Rev. Mater.* **3**, 38–51 (2018).
- Robledo, L. et al. High-fidelity projective read-out of a solid-state spin quantum register. *Nature* **477**, 574–578 (2011).
- Childress, L. et al. Coherent dynamics of coupled electron and nuclear spin qubits in diamond. *Science* **314**, 281–285 (2006).
- Humphreys, P. C. et al. Deterministic delivery of remote entanglement on a quantum network. *Nature* **558**, 268–273 (2018).
- Jarmola, A., Acosta, V. M., Jensen, K., Chemerisov, S. & Budker, D. Temperature- and magnetic-field-dependent longitudinal spin relaxation in nitrogen-vacancy ensembles in diamond. *Phys. Rev. Lett.* **108**, 197601 (2012).
- Astner, T. et al. Solid-state electron spin lifetime limited by phononic vacuum modes. *Nat. Mater.* **17**, 313–317 (2018).
- Zhao, N. et al. Sensing single remote nuclear spins. *Nat. Nanotech.* **7**, 657–662 (2012).
- Balasubramanian, G. et al. Ultralong spin coherence time in isotopically engineered diamond. *Nat. Mater.* **8**, 383–387 (2009).
- Bar-Gill, N., Pham, L. M., Jarmola, A., Budker, D. & Walsworth, R. L. Solid-state electronic spin coherence time approaching one second. *Nat. Commun.* **4**, 1743 (2012).
- Neumann, P. et al. Multipartite entanglement among single spins in diamond. *Science* **320**, 1326–1329 (2008).
- Fuchs, G. D., Burkard, G., Klimov, P. V. & Awschalom, D. D. A quantum memory intrinsic to single nitrogen-vacancy centres in diamond. *Nat. Phys.* **7**, 789–793 (2011).
- Dréau, A., Maze, J. R., Lesik, M., Roch, J. F. & Jacques, V. High-resolution spectroscopy of single NV defects coupled with nearby  $^{13}\text{C}$  nuclear spins in diamond. *Phys. Rev. B* **85**, 134107 (2012).
- Jelezko, F. et al. Observation of coherent oscillation of a single nuclear spin and realization of a two-qubit conditional quantum gate. *Phys. Rev. Lett.* **93**, 130501 (2004).
- Waldherr, G. et al. Quantum error correction in a solid-state hybrid spin register. *Nature* **506**, 204–207 (2014).
- Neumann, P. et al. Single-shot readout of a single nuclear spin. *Science* **329**, 542–544 (2010).
- Maurer, P. C. et al. Room-temperature quantum bit memory exceeding one second. *Science* **336**, 1283–1286 (2012).
- Pfender, M. et al. Protecting a diamond quantum memory by charge state control. *Nano Lett.* **17**, 5931–5937 (2017).
- Jacques, V. et al. Dynamic polarization of single nuclear spins by optical pumping of nitrogen-vacancy color centers in diamond at room temperature. *Phys. Rev. Lett.* **102**, 057403 (2009).
- Falk, A. L. et al. Optical polarization of nuclear spins in silicon carbide. *Phys. Rev. Lett.* **114**, 247603 (2015).
- Ivány, V. et al. Theoretical model of dynamic spin polarization of nuclei coupled to paramagnetic point defects in diamond and silicon carbide. *Phys. Rev. B* **92**, 115206 (2015).
- Reiserer, A. et al. Robust quantum-network memory using decoherence-protected subspaces of nuclear spins. *Phys. Rev. X* **6**, 021040 (2016).
- Kolkowitz, S., Unterreithmeier, Q. P., Bennett, S. D. & Lukin, M. D. Sensing distant nuclear spins with a single electron spin. *Phys. Rev. Lett.* **109**, 137601 (2012).
- Taminiau, T. H. et al. Detection and control of individual nuclear spins using a weakly coupled electron spin. *Phys. Rev. Lett.* **109**, 137602 (2012).
- Taminiau, T. H., Cramer, J., van der Sar, T., Dobrovitski, V. V. & Hanson, R. Universal control and error correction in multi-qubit spin registers in diamond. *Nat. Nanotech.* **9**, 171–176 (2014).
- Liu, G.-Q. et al. Single-shot readout of a nuclear spin weakly coupled to a nitrogen-vacancy center at room temperature. *Phys. Rev. Lett.* **118**, 150504 (2017).
- Dolde, F. et al. Room-temperature entanglement between single defect spins in diamond. *Nat. Phys.* **9**, 139–143 (2013).
- Staudacher, T. et al. Nuclear magnetic resonance spectroscopy on a (5-nanometer)<sup>3</sup> sample volume. *Science* **339**, 561–563 (2013).
- Mamin, H. J. et al. Nanoscale nuclear magnetic resonance with a nitrogen-vacancy spin sensor. *Science* **339**, 557–560 (2013).
- Barclay, P. E., Fu, K.-M. C., Santori, C., Faraon, A. & Beausoleil, R. G. Hybrid nanocavity resonant enhancement of color center emission in diamond. *Phys. Rev. X* **1**, 011007 (2011).
- Faraon, A., Santori, C., Huang, Z., Acosta, V. M. & Beausoleil, R. G. Coupling of nitrogen-vacancy centers to photonic crystal cavities in monocrystalline diamond. *Phys. Rev. Lett.* **109**, 033604 (2012).
- Aharonovich, I. & Neu, E. Diamond nanophotonics. *Adv. Opt. Mater.* **2**, 911–928 (2014).
- Schröder, T. et al. Quantum nanophotonics in diamond. *J. Opt. Soc. Am. B* **33**, B65–B83 (2016).
- Zaske, S. et al. Visible-to-telecom quantum frequency conversion of light from a single quantum emitter. *Phys. Rev. Lett.* **109**, 147404 (2012).
- Riedel, D. et al. Deterministic enhancement of coherent photon generation from a nitrogen-vacancy center in ultrapure diamond. *Phys. Rev. X* **7**, 031040 (2017).
- Dréau, A., Tchekorava, A., El Mahdaoui, A., Bonato, C. & Hanson, R. Quantum frequency conversion to telecom of single photons from a nitrogen-vacancy center in diamond. *Phys. Rev. Appl.* **9**, 064031 (2018).
- Hepp, C. et al. Electronic structure of the silicon vacancy color center in diamond. *Phys. Rev. Lett.* **112**, 036405 (2014).
- Rogers, L. J. et al. Multiple intrinsically identical single-photon emitters in the solid state. *Nat. Commun.* **5**, 4739 (2014).
- Pingault, B. et al. All-optical formation of coherent dark states of silicon-vacancy spins in diamond. *Phys. Rev. Lett.* **113**, 263601 (2014).
- Rogers, L. J. et al. All-optical initialization, readout, and coherent preparation of single silicon-vacancy spins in diamond. *Phys. Rev. Lett.* **113**, 263602 (2014).
- Pingault, B. et al. Coherent control of the silicon-vacancy spin in diamond. *Nat. Commun.* **8**, 15579 (2017).
- Becker, J. N. et al. All-optical control of the silicon-vacancy spin in diamond at millikelvin temperatures. *Phys. Rev. Lett.* **120**, 053603 (2018).
- Sukachev, D. D. et al. Silicon-vacancy spin qubit in diamond: a quantum memory exceeding 10 ms with single-shot state readout. *Phys. Rev. Lett.* **119**, 223602 (2017).
- Rogers, L. J. et al. Electronic structure of the negatively charged silicon-vacancy center in diamond. *Phys. Rev. B* **89**, 235101 (2014).
- Sipahigil, A. et al. An integrated diamond nanophotonics platform for quantum-optical networks. *Science* **354**, 847–850 (2016).
- Bhaskar, M. K. et al. Quantum nonlinear optics with a germanium-vacancy color center in a nanoscale diamond waveguide. *Phys. Rev. Lett.* **118**, 223603 (2017).
- Siyushev, P. et al. Optical and microwave control of germanium-vacancy center spins in diamond. *Phys. Rev. B* **96**, 081201 (2017).
- Green, B. L. et al. Neutral silicon-vacancy center in diamond: spin polarization and lifetimes. *Phys. Rev. Lett.* **119**, 096402 (2017).
- Rose, B. C. et al. Observation of an environmentally insensitive solid state spin defect in diamond. *Science* **361**, 60–63 (2018).
- Tchernij, S. D. et al. Single-photon-emitting optical centers in diamond fabricated upon Sn implantation. *ACS Photon.* **4**, 2580–2586 (2017).

66. Iwasaki, T. et al. Tin-vacancy quantum emitters in diamond. *Phys. Rev. Lett.* **119**, 253601 (2017).
67. Koehl, W. F., Buckley, B. B., Heremans, F. J., Calusine, G. & Awschalom, D. D. Room temperature coherent control of defect spin qubits in silicon carbide. *Nature* **479**, 84–87 (2011).
68. Falk, A. L. et al. Polytype control of spin qubits in silicon carbide. *Nat. Commun.* **4**, 1819 (2013).
69. Falk, A. L. et al. Electrically and mechanically tunable electron spins in silicon carbide color centers. *Phys. Rev. Lett.* **112**, 187601 (2014).
70. Whiteley, S. J. et al. Probing spin-phonon interactions in silicon carbide with Gaussian acoustics. Preprint at <https://arxiv.org/abs/1804.10996> (2018).
71. Klimov, P. V., Falk, A. L., Christle, D. J., Dobrovitski, V. V. & Awschalom, D. D. Quantum entanglement at ambient conditions in a macroscopic solid-state spin ensemble. *Sci. Adv.* **1**, e1501015 (2015).
72. Christle, D. J. et al. Isolated electron spins in silicon carbide with millisecond coherence times. *Nat. Mater.* **14**, 160–163 (2014).
73. Simin, D. et al. Locking of electron spin coherence above 20 ms in natural silicon carbide. *Phys. Rev. B* **95**, 161201 (2017).
74. Nagy, R. et al. Quantum properties of dichroic silicon vacancies in silicon carbide. *Phys. Rev. Appl.* **9**, 034022 (2018).
75. Widmann, M. et al. Coherent control of single spins in silicon carbide at room temperature. *Nat. Mater.* **14**, 164–168 (2014).
76. Yang, L.-P. et al. Electron spin decoherence in silicon carbide nuclear spin bath. *Phys. Rev. B* **90**, 241203 (2014).
77. Seo, H. et al. Quantum decoherence dynamics of divacancy spins in silicon carbide. *Nat. Commun.* **7**, 12935 (2016).
78. Christle, D. J. et al. Isolated spin qubits in SiC with a high-fidelity infrared spin-to-photon interface. *Phys. Rev. X* **7**, 021046 (2017).
79. de las Casas, C. F. et al. Stark tuning and electrical charge state control of single divacancies in silicon carbide. *Appl. Phys. Lett.* **111**, 262403 (2017).
80. Radulaski, M. et al. Photonic crystal cavities in cubic (3C) polytype silicon carbide films. *Opt. Express* **21**, 32623–32629 (2013).
81. Calusine, G., Politi, A. & Awschalom, D. D. Cavity-enhanced measurements of defect spins in silicon carbide. *Phys. Rev. Appl.* **6**, 014019 (2016).
82. Soykal, O., Dev, P. & Economou, S. E. Silicon vacancy center in 4H-SiC: electronic structure and spin-photon interfaces. *Phys. Rev. B* **93**, 081207(R) (2016).
83. Kraus, H. et al. Magnetic field and temperature sensing with atomic-scale spin defects in silicon carbide. *Sci. Rep.* **4**, 5303 (2014).
84. Niethammer, M. et al. Vector magnetometry using silicon vacancies in 4H-SiC under ambient conditions. *Phys. Rev. Appl.* **6**, 034001 (2016).
85. Heshami, K. et al. Quantum memories: emerging applications and recent advances. *J. Mod. Opt.* **63**, 2005–2028 (2016).
86. Könz, F. et al. Temperature and concentration dependence of optical dephasing, spectral-hole lifetime, and anisotropic absorption in  $\text{Eu}^{3+}:\text{Y}_2\text{SiO}_5$ . *Phys. Rev. B* **68**, 085109 (2003).
87. Zhong, M. et al. Optically addressable nuclear spins in a solid with a six-hour coherence time. *Nature* **517**, 177–180 (2015).
88. O'Brien, C., Lauk, N., Blum, S., Morigi, G. & Fleischhauer, M. Interfacing superconducting qubits and telecom photons via a rare-earth-doped crystal. *Phys. Rev. Lett.* **113**, 063603 (2014).
89. Williamson, L. A., Chen, Y.-H. & Longdell, J. J. Magneto-optic modulator with unit quantum efficiency. *Phys. Rev. Lett.* **113**, 203601 (2014).
90. Utikal, T. et al. Spectroscopic detection and state preparation of a single praseodymium ion in a crystal. *Nat. Commun.* **5**, 3627 (2014).
91. Eichhammer, E., Utikal, T., Göttinger, S. & Sandoghdar, V. Spectroscopic detection of single  $\text{Pr}^{3+}$  ions on the  $^3\text{H}_4$   $\rightarrow$   $^1\text{D}_2$  transition. *New J. Phys.* **17**, 083018 (2015).
92. Nakamura, I., Yoshihiro, T., Inagawa, H., Fujiyoshi, S. & Matsushita, M. Spectroscopy of single  $\text{Pr}^{3+}$  ion in  $\text{LaF}_3$  crystal at 1.5 K. *Sci. Rep.* **4**, 7364 (2015).
93. Kolesov, R. et al. Optical detection of a single rare-earth ion in a crystal. *Nat. Commun.* **3**, 1029 (2012).
94. Siyushev, P. et al. Coherent properties of single rare-earth spin qubits. *Nat. Commun.* **5**, 3895 (2014).
95. Xia, K. et al. Optical and spin properties of a single praseodymium ion in a crystal. Preprint at <http://arxiv.org/abs/1706.08736> (2017).
96. Fraval, E., Sellars, M. J. & Longdell, J. J. Dynamic decoherence control of a solid-state nuclear-quadrupole qubit. *Phys. Rev. Lett.* **95**, 030506 (2005).
97. Yin, C. et al. Optical addressing of an individual erbium ion in silicon. *Nature* **497**, 91–94 (2013).
98. Zhong, T. et al. Nanophotonic rare-earth quantum memory with optically controlled retrieval. *Science* **357**, 1392–1395 (2017).
99. Zhong, T. et al. Optically addressing single rare-earth ions in a nanophotonic cavity. Preprint at <http://arxiv.org/abs/1803.07520> (2018).
100. Dibos, A., Raha, M., Phenicie, C. & Thompson, J. Isolating and enhancing the emission of single erbium ions using a silicon nanophotonic cavity. *Phys. Rev. Lett.* **120**, 243601 (2018).
101. Muhonen, J. T. et al. Storing quantum information for 30 seconds in a nanoelectronic device. *Nat. Nanotech.* **9**, 986–991 (2014).
102. Tosi, G., Mohiyaddin, F. A., Huebl, H. & Morello, A. Circuit-quantum electrodynamics with direct magnetic coupling to single-atom spin qubits in isotopically enriched  $^{28}\text{Si}$ . *AIP Adv.* **4**, 087122 (2014).
103. Morse, K. J. et al. A photonic platform for donor spin qubits in silicon. *Sci. Adv.* **3**, e1700930 (2017).
104. Mi, X. et al. A coherent spin-photon interface in silicon. *Nature* **555**, 599–603 (2018).
105. Samkharadze, N. et al. Strong spin-photon coupling in silicon. *Science* **359**, 1123–1127 (2018).
106. Steger, M. et al. Quantum information storage for over 180 s using donor spins in a  $^{28}\text{Si}$  ‘semiconductor vacuum’. *Science* **336**, 1280–1283 (2012).
107. Saeedi, K. et al. Room-temperature quantum bit storage exceeding 39 minutes using ionized donors in silicon-28. *Science* **342**, 830–833 (2013).
108. Vazirani, U. & Vidick, T. Fully device-independent quantum key distribution. *Phys. Rev. Lett.* **113**, 140501 (2014).
109. Barz, S. et al. Demonstration of blind quantum computing. *Science* **335**, 303–308 (2012).
110. Hensen, B. et al. Loophole-free Bell inequality violation using electron spins separated by 1.3 kilometres. *Nature* **526**, 682–686 (2015).
111. Pfaff, W. et al. Unconditional quantum teleportation between distant solid-state quantum bits. *Science* **345**, 532–535 (2014).
112. Kalb, N. et al. Entanglement distillation between solid-state quantum network nodes. *Science* **356**, 928–932 (2017).
113. Yang, S. et al. High-fidelity transfer and storage of photon states in a single nuclear spin. *Nat. Photon.* **10**, 507–511 (2016).
114. Heshami, K. et al. Raman quantum memory based on an ensemble of nitrogen-vacancy centers coupled to a microcavity. *Phys. Rev. A* **89**, 040301 (2014).
115. Poem, E. et al. Broadband noise-free optical quantum memory with neutral nitrogen-vacancy centers in diamond. *Phys. Rev. B* **91**, 205108 (2015).
116. Kosaka, H. & Niikura, N. Entangled absorption of a single photon with a single spin in diamond. *Phys. Rev. Lett.* **114**, 053603 (2015).
117. Monroe, C. et al. Large-scale modular quantum-computer architecture with atomic memory and photonic interconnects. *Phys. Rev. A* **89**, 022317 (2014).
118. Nickerson, N. H., Li, Y. & Benjamin, S. C. Topological quantum computing with a very noisy network and local error rates approaching one percent. *Nat. Commun.* **4**, 1756 (2013).
119. Cramer, J. et al. Repeated quantum error correction on a continuously encoded qubit by real-time feedback. *Nat. Commun.* **7**, 11526 (2016).
120. Cai, J., Retzker, A., Jelezko, F. & Plenio, M. B. A large-scale quantum simulator on a diamond surface at room temperature. *Nat. Phys.* **9**, 168–173 (2013).
121. Wang, Y. et al. Quantum simulation of helium hydride cation in a solid-state spin register. *ACS Nano* **9**, 7769–7774 (2015).
122. Kong, F. et al. Direct measurement of topological numbers with spins in diamond. *Phys. Rev. Lett.* **117**, 060503 (2016).
123. Le Sage, D. et al. Optical magnetic imaging of living cells. *Nature* **496**, 486–489 (2013).
124. Simpson, D. A. et al. Non-neurotoxic nanodiamond probes for intraneuronal temperature mapping. *ACS Nano* **11**, 12077–12086 (2017).
125. Thiel, L. et al. Quantitative nanoscale vortex imaging using a cryogenic quantum magnetometer. *Nat. Nanotech.* **11**, 677–681 (2016).
126. Pelliccione, M. et al. Scanned probe imaging of nanoscale magnetism at cryogenic temperatures with a single-spin quantum sensor. *Nat. Nanotech.* **11**, 700–705 (2016).
127. Gross, I. et al. Real-space imaging of non-collinear antiferromagnetic order with a single-spin magnetometer. *Nature* **549**, 252–256 (2017).
128. Barry, J. F. et al. Optical magnetic detection of single-neuron action potentials using quantum defects in diamond. *Proc. Natl Acad. Sci. USA* **113**, 14133–14138 (2016).
129. Shi, F. et al. Single-protein spin resonance spectroscopy under ambient conditions. *Science* **347**, 1135–1138 (2015).
130. Lovchinsky, I. et al. Nuclear magnetic resonance detection and spectroscopy of single proteins using quantum logic. *Science* **351**, 836–841 (2016).
131. Casola, F., van der Sar, T. & Yacoby, A. Probing condensed matter physics with magnetometry based on nitrogen-vacancy centres in diamond. *Nat. Rev. Mater.* **3**, 17088 (2018).
132. Appel, P., Ganzhorn, M., Neu, E. & Maletinsky, P. Nanoscale microwave imaging with a single electron spin in diamond. *New J. Phys.* **17**, 112001 (2015).
133. Jakobi, I. et al. Measuring broadband magnetic fields on the nanoscale using a hybrid quantum register. *Nat. Nanotech.* **12**, 67–72 (2016).
134. Laraoui, A. et al. High-resolution correlation spectroscopy of  $^{13}\text{C}$  spins near a nitrogen-vacancy centre in diamond. *Nat. Commun.* **4**, 1651 (2013).
135. Kong, X., Stark, A., Du, J., McGuinness, L. P. & Jelezko, F. Towards chemical structure resolution with nanoscale nuclear magnetic resonance spectroscopy. *Phys. Rev. Appl.* **4**, 024004 (2015).

136. Zaiser, S. et al. Enhancing quantum sensing sensitivity by a quantum memory. *Nat. Commun.* **7**, 12279 (2016).
137. Pfender, M. et al. Nonvolatile nuclear spin memory enables sensor-unlimited nanoscale spectroscopy of small spin clusters. *Nat. Commun.* **8**, 834 (2017).
138. Rosskopf, T., Zopes, J., Boss, J. M. & Degen, C. L. A quantum spectrum analyzer enhanced by a nuclear spin memory. *npj Quantum Inf.* **3**, 33 (2017).
139. Aslam, N. et al. Nanoscale nuclear magnetic resonance with chemical resolution. *Science* **357**, 67–71 (2017).
140. Glenn, D. R. et al. High-resolution magnetic resonance spectroscopy using a solid-state spin sensor. *Nature* **555**, 351–354 (2018).
141. Boss, J. M., Cuijia, K. S., Zopes, J. & Degen, C. L. Quantum sensing with arbitrary frequency resolution. *Science* **356**, 837–840 (2017).
142. Schmitt, S. et al. Submillihertz magnetic spectroscopy performed with a nanoscale quantum sensor. *Science* **356**, 832–837 (2017).
143. Astner, T. et al. Coherent coupling of remote spin ensembles via a cavity bus. *Phys. Rev. Lett.* **118**, 140502 (2017).
144. Barfuss, A., Teissier, J., Neu, E., Nunnenkamp, A. & Maletinsky, P. Strong mechanical driving of a single electron spin. *Nat. Phys.* **11**, 820–824 (2015).
145. Lee, D., Lee, K. W., Cady, J. V., Ovarthaiyapong, P. & Jayich, A. C. B. Topical review: spins and mechanics in diamond. *J. Opt.* **19**, 033001 (2017).
146. Wolfe, C. S. et al. Off-resonant manipulation of spins in diamond via precessing magnetization of a proximal ferromagnet. *Phys. Rev. B* **89**, 180406 (2014).
147. Andrich, P. et al. Long-range spin wave mediated control of defect qubits in nanodiamonds. *npj Quantum Inf.* **3**, 28 (2017).
148. Najafi, F. et al. On-chip detection of non-classical light by scalable integration of single-photon detectors. *Nat. Commun.* **6**, 5873 (2015).
149. Grote, R. R. et al. Imaging a nitrogen-vacancy center with a diamond immersion metalens. Preprint at <http://arxiv.org/abs/1711.00901> (2017).
150. Steinert, S. et al. Magnetic spin imaging under ambient conditions with sub-cellular resolution. *Nat. Commun.* **4**, 1607 (2013).
151. Fedotov, I. V. et al. Electron spin manipulation and readout through an optical fiber. *Sci. Rep.* **4**, 5362 (2015).
152. Kehayias, P. et al. Solution nuclear magnetic resonance spectroscopy on a nanostructured diamond chip. *Nat. Commun.* **8**, 188 (2017).
153. van Dam, S. B., Humphreys, P. C., Rozpędek, F., Wehner, S. & Hanson, R. Multiplexed entanglement generation over quantum networks using multi-qubit nodes. *Quantum Sci. Technol.* **2**, 034002 (2017).
154. Geng, J. et al. Experimental time-optimal universal control of spin qubits in solids. *Phys. Rev. Lett.* **117**, 170501 (2016).
155. Zhou, B. B. et al. Accelerated quantum control using superadiabatic dynamics in a solid-state lambda system. *Nat. Phys.* **13**, 330–334 (2017).
156. Hirose, M. & Cappellaro, P. Coherent feedback control of a single qubit in diamond. *Nature* **532**, 77–80 (2016).
157. Uden, T. et al. Quantum metrology enhanced by repetitive quantum error correction. *Phys. Rev. Lett.* **116**, 230502 (2016).
158. Lesik, M. et al. Perfect preferential orientation of nitrogen-vacancy defects in a synthetic diamond sample. *Appl. Phys. Lett.* **104**, 113107 (2014).
159. Michl, J. et al. Perfect alignment and preferential orientation of nitrogen-vacancy centers during chemical vapor deposition diamond growth on (111) surfaces. *Appl. Phys. Lett.* **104**, 102407 (2014).
160. Fukui, T. et al. Perfect selective alignment of nitrogen-vacancy centers in diamond. *Appl. Phys. Express* **7**, 055201 (2014).

## Acknowledgements

We thank A. Crook, F. J. Heremans, P. Jerger, K. Miao, T. Taminiau, G. Wolfowicz and T. Zhong for illuminating discussions. D.D.A. and B.B.Z. acknowledge support from the National Science Foundation grant EFMA-164109, the Air Force Office of Scientific Research grants FA9550-14-1-0231 and FA9550-15-1-0029, and the Army Research Office QSEP grant W911NF-15-2-0058. R.H. acknowledges support from the Netherlands Organisation for Scientific Research (NWO) through a VICI grant and the European Research Council (ERC) through a Consolidator Grant. J.W. acknowledges support from ERC grant SMel, the BW foundation, BMBF grant BrainQSens, and the Max Planck Society.

## Competing interests

The authors declare no competing interests.

## Additional information

Reprints and permissions information is available at [www.nature.com/reprints](http://www.nature.com/reprints).

Correspondence should be addressed to D.D.A.

**Publisher's note:** Springer Nature remains neutral with regard to jurisdictional claims in published maps and institutional affiliations.